Investigation of La^{3+} Doped $Yb_2Sn_2O_7$ as New Thermal Barrier Materials

Jing Wang[1], Fang Xu[1], Richard J. Wheatley[2], Kwang-Leong Choy[1], Nigel Neate[1], Xianghui Hou[1*]

[1]*Department of Mechanical, Materials and Manufacturing Engineering, University of Nottingham, Nottingham, NG7 2RD, UK*

[2] *School of Chemistry, University of Nottingham, Nottingham, NG7 2RD, UK*

Materials & Design, Volume 85, 15 November 2015, Pages 423–430
doi:10.1016/j.matdes.2015.07.022

Abstract

Low thermal conductivity is one of the key requirements for thermal barrier coating materials. From the consideration of crystal structure and ion radius, La^{3+} Doped $Yb_2Sn_2O_7$ ceramics with pyrochlore crystal structures were synthesised by sol-gel method as candidates of thermal barrier materials in aero-engines. As La^{3+} and Yb^{3+} ions have the largest radius difference in lanthanoids group, La^{3+} ions were expected to produce significant disorders by replacing Yb^{3+} ions in cation layers of $Yb_2Sn_2O_7$. Both experimental and computational phase analysis were carried out, and good agreement had been obtained. The lattice constants of solid solution $(La_xYb_{1-x})_2Sn_2O_7$ (x=0.3, 0.5, 0.7) increased linearly when the content of La^{3+} was increased. The thermal properties (thermal conductivity and coefficients of thermal expansion) of the synthesized materials had been compared with traditional 8 wt.% Yttria Stabilized Zirconia (8YSZ) and $La_2Zr_2O_7$ (LZ). It was found that La^{3+} Doped $Yb_2Sn_2O_7$ exhibited lower thermal conductivities than un-doped stannates. Amongst all compositions studied, $(La_{0.5}Yb_{0.5})_2Sn_2O_7$ exhibited the lowest thermal conductivity (0.851 $W{\cdot}m^{-1}{\cdot}K^{-1}$ at room temperature), which was much lower than that of 8YSZ (1.353 $W{\cdot}m^{-1}{\cdot}K^{-1}$), and possessed a high coefficient of thermal expansion (CTE), 13.530×10^{-6} K^{-1} at 950°C.

Keywords: Sol-gel; Thermal barrier coating; Thermal conductivity; Coefficient of thermal expansion

*Corresponding Author, email: xianghui.hou@nottingham.ac.uk

1 Introduction

Thermal barrier coatings (TBCs) are a kind of thermal insulating materials applied to the surface of super nickel alloy substrates, to protect them from high temperature environment in aero-engines, and improve thermal cyclic life and reduce oxidation [1, 2]. TBCs consist of three layers: bond coat (BC), top coat (TC) and thermal grown oxide (TGO) layer, the thickness of which increased between BC and TC after long thermal cycles. 7-8 wt.% ytrria-stablized zirconia (7-8YSZ) has been well studied and applied as a top ceramic layer for several decades. However, the traditional 7-8YSZ materials have the limitation of poor thermal phase stability after long thermal cycling at high temperature (above 1200^{o}C), as well as their relatively high thermal conductivities [3-6]. Therefore, there is a strong need to develop new candidate materials with lower conductivities and good phase stability to enhance the efficiency of gas engines. So far, there are many new materials with complex crystal structures that have been investigated for thermal barrier coating application, such as pyrochlore, magnetoplumbite, perovskite, and garnet [7-11]. Stannates with pyrochlore structure have good phase stability up to their melting points (>2000^{o}C) [12, 13], which is much higher than that of 8YSZ (~1200^{o}C). Recently, Shelling *et al.* found that pyrochlore might have much lower thermal conductivity than other systems [14]. From their simulation results, stannates were predicted to have the lowest thermal conductivity in pyrochlores, though the low coefficients of thermal expansion (CTEs) of stannates need further improvement for TBC application.

Furthermore, the thermal properties of un-doped stannates were studied by Qu *et al.* [15]. $Ln_2Sn_2O_7$ (Ln = La, Nd, Sm, Gd, Er and Yb) samples prepared by a chemical co-precipitation method exhibited the pyrochlore crystal structure. However, their thermal conductivities were

above 2 $W \cdot m^{-1} \cdot K^{-1}$ at 1200°C, and their CTEs ($7 \sim 9 \times 10^{-6}$ K^{-1}) were slightly lower than YSZ. These lower thermal conductivity values were explained in terms of scattering the phonons by the strain field caused by the displacement of 48*f* oxygen ions in the pyrochlore crystal structure, rather than oxygen vacancies at 8*a* sites.

Bansal *et al.* [16] found that small amount of rare earth doped pyrochlore had relatively low thermal conductivity, but the value was still above 1 $W \cdot m^{-1} \cdot K^{-1}$. In ceramic materials, phonons carry heat energy due to thermal motion of atoms (vibrations in different directions), which plays a main role on thermal conductivity [17]. In a perfect and simple crystal, the vibrations of atoms are monotonous and independent of each other, so thermal conductivity can be infinite. But in the real case, there are defects, distortions, and strain *etc.* in crystals, which have significant effects on thermal conductivity due to scattering phonons.

In the past, most studies were based on un-doped stannates. In the present work, based on the consideration of crystal structure and the relative ion radius, La^{3+} Doped $Yb_2Sn_2O_7$ materials have been systematically investigated. As La^{3+} ions (0.118 nm) have larger radius than Yb^{3+} (0.098 nm) [18], it is expected to produce significantly disorders by replacing Yb^{3+} ions in cation layers, and these disorders could have huge effects on the thermal properties of the materials.

2 Experimental work

2.1 Preparation of ceramic powders

Sol-gel method was used to synthesize ceramic powders as TBC candidates. Rare earth nitrates (Sigma-Aldrich, 99.8~99.9%) and stannic chloride (Sigma-Aldrich, 98%) were selected as raw materials and citric acid (Sigma-Aldrich, 99%) as organic complexing agent. Methanol (Sigma-Aldrich, ≥99.8%) was used as solvent. Firstly, a certain amount of stannic chloride determined by different stoichiometric ratios of ceramics was dissolved in methanol, followed by slowly dropping rare earth nitrate solutions under magnetic stirring. After stirring for 30 mins, citric acid was added at a molar ratio of citric acid/cation ions = 1.2:1.0. The forerunner was stirred for 6 h at room temperature and then held under static condition at 50^{o}C for two days until gel formed. Then the gels were dried at 120^{o}C. Afterwards, dried gels were placed into alumina crucible, and heated to 500^{o}C with a heating rate of 2 ^{o}C/min and kept for 5 h to remove organic compositions; then the intermediates were heated up to 950^{o}C with a rate of 5 ^{o}C/min, and held for 4 h, to completely remove other impurities, such as nitrate groups. The next step was to further crystalize the materials at 1300^{o}C for 6 h, with heating rate of 10 ^{o}C/min and cooling rate of 30 ^{o}C/min. Then the products were ground to ceramic powders with a mortar. At last, pellets with diameters of 20 mm and 5 mm, were separately compressed under fixed pressure (~130 MPa for ϕ20 mm and ~32 MPa for ϕ5 mm pellets, respectively) by a Pellet Press (Specac) and sintered at 1300^{o}C for 6 h, at a heating rate of 10 ^{o}C/min and cooling rate of 15 ^{o}C/min.

8 wt.% YSZ and $La_2Zr_2O_7$ were synthesized as the reference materials. Yttrium and lanthanum nitrates (Sigma-Aldrich, 99~99.8%) and zirconyl chloride octahydrate (Sigma-Aldrich, 98%) were chosen as raw materials and citric acid as organic complexing agent. The e molar ratio of citric acid/cation ions for 8YSZ was 0.6:1.0. Then similar process as the stannates was carried out to form the reference powder and pellets.

2.2 Characterization

X-Ray Diffraction (XRD, Siemens D500) using *Cu K*-alpha radiation as X-Ray source was used to analyse the crystalline phase at room temperature, with scanning range of 2-theta (2θ) from 20^o to 90^o and scanning step of 0.02^o. The applied voltage and current were 40 kV and 25 mA, respectively. The XRD results were analysed by Eva software. For better understanding the crystal structure of $(La_xYb_{1-x})_2Sn_2O_7$ (x=0.3, 0.5, 0.7) solid solution, Rietveld refinement was applied to calculate the lattice constants of $(La_xYb_{1-x})_2Sn_2O_7$ (x=0.3, 0.5, 0.7) and the relative phase contents in $(La_xYb_{1-x})_2Sn_2O_7$ by using the third Chu-Wan profile (CW profile) function of General Structure Analysis System (GSAS) software [19]. The calculative XRD database was referenced from pyrochlore $La_2Zr_2O_7$ [20].

The microstructures of ceramic powders were studied by Transmission Electron Microscopy (TEM). The TEM specimens were prepared by dispersing small amount of ceramic powders in pure alcohol in an ultrasonic generator, and placing a drop of the dispersion on a copper mesh covered with a 'holey' carbon film. Conventional TEM images and electron diffraction patterns were obtained from JEOL 2000FX operated at 200 kV.

Thermal Conductivity Analyser (TCA, C-THERM Tci^{TM}) was used to detect thermal conductivities of ceramic pellets with ~20 mm in diameters and minimum thickness of 3 mm at room temperature. Wakefield solution of T120 silicone was applied between the ceramic pellet and a sensor as thermal joint compound for good contact. One thermal conductivity value was obtained from 10 time measurement, and the average values were used in this study. The thermal conductivities of all pellets were corrected from the measured thermal conductivities and their porosities by equation (1) [21]:

$$\frac{k}{k_o} = 1 - \frac{4}{3}\emptyset, \qquad (1)$$

where k was the value of measured thermal conductivity using TCA equipment; k_o was the

corrected value of sample and Ø was the estimated fractional porosity of specimen.

The porosities of pellets were obtained from the relative density calculated by equation (2). The measured density (ρ) of each pellet was calculated by the weight and the volume. The theory density (ρ_{th}) of each pellet was calculated using equation (3) [22]. The volume of unit cell was calculated from lattice parameters as obtained from XRD results.

$$\emptyset = 1 - \rho = 1 - \frac{\rho}{\rho_{th}}, \qquad (2)$$

$$\rho_{th} = \frac{(MW)(n)}{V_{cell}N_A} \times 10^{27}, \qquad (3)$$

where MW was molecular weight; n was formula unit per unit cell; V_{cell} was volume of the unit cell ; N_A was Avogadro constant, 6.022×10^{23}. Therefore, all thermal conductivities discussed in this work are the values after correction.

Thermal Mechanical Analysis (TMA) Q400 was used to measure the CTEs of the ceramic pellets. The diameters of the testing pellets were 5 mm, the preload was 0.05 N and the applied force was 0.02 N. The measurement was carried out in nitrogen atmosphere with a N_2 flow rate of 50 mL/min from room temperature to 950^{o}C.

3 Results and Discussion

3.1 Pyrochlore structure and strategy to reduce thermal conductivity

Pyrochlore is a derivation of fluorite structure [23], where a quarter part of pyrochlore has similar structure to fluorite unit cell and the difference is 8a vacancies created by missing oxygen atoms in pyrochlore. Pyrochlore has cubic crystal structure, which is stable from room temperature up to its melting point [12, 13]. This property is the key advantage for gas engine application at high temperatures. As shown in Figure 1**(a)**, oxygen atoms locate between cation layers but some of them are displaced from their centre positions due to the

nearby oxygen vacancies at 8*a* sites. The sub-lattice of cations [Figure 1**(b)**] shows layered-crystal structure that is more helpful for scattering phonons. If substitutional defects of cations and disorders are created between these layers, it could be a useful strategy to further reduce thermal conductivity of pyrochlore material. In lanthanoids group, La^{3+} and Yb^{3+} ions have the biggest radius difference, so by doping La^{3+} to replace Yb^{3+}, the most serious disorders would be produced in cation layers of crystal $Yb_2Sn_2O_7$.

3.2 Experimental and computational XRD data and phase analysis

In Figure 2, XRD patterns of $La_2Zr_2O_7$, $La_2Sn_2O_7$, $(La_{0.7}Yb_{0.3})_2Sn_2O_7$, $(La_{0.5}Yb_{0.5})_2Sn_2O_7$, $(La_{0.3}Yb_{0.7})_2Sn_2O_7$ and $Yb_2Sn_2O_7$ indicate their crystal structures. Figure 2 **(a)** presents pyrochlore crystal structures, distinguished from fluorite by (3,3,1) and (5,1,1) peaks, which is in good agreement with the previous report by Brisse and Knop [24]. They have good phase stability even at very high temperature, due to their pyrochlore structure [12, 13]. A minor second phase La_2O_3 is detected in $La_2Sn_2O_7$, $(La_{0.7}Yb_{0.3})_2Sn_2O_7$ and $(La_{0.5}Yb_{0.5})_2Sn_2O_7$ powders. In Figure 2 **(b)**, by increasing the doping contents of Yb^{3+} to replace La^{3+} ions, the lattice parameters are continuously decreasing [10], which can be observed from (2,2,2), (4,0,0), (4,4,0) and (6,2,2) peaks that are shifting from low 2θ. In addition, it is found that there are two compositions in solid solution $(La_xYb_{1-x})_2Sn_2O_7$ (x=0.3, 0.5 and 0.7) by distinguishing the overlapped two peaks, (4,4,0) and (6,2,2). In order to identify these compositions, C1 and C2 [$(La_{0.7}Yb_{0.3})_2Sn_2O_7$], C3 and C4 [$(La_{0.5}Yb_{0.5})_2Sn_2O_7$], C5 and C6 [$(La_{0.3}Yb_{0.7})_2Sn_2O_7$], are introduced to represent these different compositions, which also have a pyrochlore crystal structure.

According to Rietveld refinement, Figure 3 **(a)-(c)** demonstrates that calculative XRD patterns of samples $(La_{0.7}Yb_{0.3})_2Sn_2O_7$, $(La_{0.5}Yb_{0.5})_2Sn_2O_7$ and $(La_{0.3}Yb_{0.7})_2Sn_2O_7$ have good

fitting agreement with their experimental XRD results, especially at high 2θ. The lattice constants and relative phase contents of C1, C2, C3, C4, C5 and C6 obtained from the simulation are listed in Table 1. It is observed that the contents of different compositions in $(La_{0.5}Yb_{0.5})_2Sn_2O_7$ and $(La_{0.3}Yb_{0.7})_2Sn_2O_7$ are slightly different from those in $(La_{0.7}Yb_{0.3})_2Sn_2O_7$. The relative phase contents of C3 (10.570 Å) and C5 (10.525 Å) are 28.10% and 21.72%, so C4 (10.483 Å) and C6 (10.432 Å) are 71.90% and 78.28%, respectively. But in sample $(La_{0.7}Yb_{0.3})_2Sn_2O_7$, the relative phase contents of C1 and C2 are 73.77% and 26.23% with lattice constants of 10.655 Å and 10.585 Å, respectively. Apparently, the relative phase contents of the compositions with larger lattice constants decrease with the decreasing doping level of La^{3+} ions. But when larger ion La^{3+} ions dominate in solid solution $(La_{0.7}Yb_{0.3})_2Sn_2O_7$, the relative phase content of composition C1 with rich La^{3+} ions is higher than that of composition C2.

According to a previous study, the lattice constant of $La_2Sn_2O_7$ is 10.631 Å [25], and 10.276 Å for $Yb_2Sn_2O_7$ [26]. Figure 4 demonstrates that the lattice constants of $(La_xYb_{1-x})_2Sn_2O_7$ (x=0.3, 0.5 and 0.7) solid solution obtained from rietveld refinement, are almost linearly increasing with the increase of the La^{3+} ions (mol.%), because the radius of La^{3+} ion (0.118 nm) is larger than that of Yb^{3+} ion (0.098 nm) [18]. Therefore, for $(La_{0.7}Yb_{0.3})_2Sn_2O_7$, $(La_{0.5}Yb_{0.5})_2Sn_2O_7$ and $(La_{0.3}Yb_{0.7})_2Sn_2O_7$ solid solutions, the La^{3+} ion contents in C1, C3 and C5 would be slightly higher than those in the corresponding compositions (C2, C4 and C6). Meanwhile, their linear slopes have similar values and the lattice constants are decreasing with the reducing contents of dopant La^{3+} ions. From microstructure level, the difference between these lattice constants could cause the strain and stress in materials, which can also be observed in the following TEM observation and might also contribute to phonon scattering for reducing their thermal conductivities, because strain and stress can cause difficulty for

phonons to travel through the lattice.

3.3 TEM analysis

Bright field TEM images and electron diffraction patterns of $Yb_2Sn_2O_7$, $(La_{0.5}Yb_{0.5})_2Sn_2O_7$, $(La_{0.7}Yb_{0.3})_2Sn_2O_7$, and $(La_{0.3}Yb_{0.7})_2Sn_2O_7$ ceramics are presented in Figure 5 **(a)-(d)**, respectively. The crystal sizes of $Yb_2Sn_2O_7$, $(La_{0.7}Yb_{0.3})_2Sn_2O_7$, $(La_{0.5}Yb_{0.5})_2Sn_2O_7$ and $(La_{0.3}Yb_{0.7})_2Sn_2O_7$ powders range from 30 nm to 100 nm. Crystals of $Yb_2Sn_2O_7$ in Figure 5 **(a)** have uniform diffraction contrast. But in **(b)**, **(c)** and **(d)**, TEM images of $(La_{0.7}Yb_{0.3})_2Sn_2O_7$, $(La_{0.5}Yb_{0.5})_2Sn_2O_7$ and $(La_{0.3}Yb_{0.7})_2Sn_2O_7$ ceramics have diffraction contrast variation, indicating the existence of strain and stress within the particles that might result from two different compositions or caused by the displacement of 48*f* oxygen ions in the pyrochlore crystal structure [15]. The *d*-spacings of ceramic $Yb_2Sn_2O_7$ are in agreement with the Powder Diffraction Pattern (PDF) data reported by Kennedy [27]. In addition, from the electron diffraction pattern insets in Figure 5, $(La_xYb_{1-x})_2Sn_2O_7$ (x=0.3, 0.5 and 0.7) solid solutions have smaller *d*-spacing values if compared with the standard $Yb_2Sn_2O_7$, as also being observed according to the peak shift to lower 2θ in XRD results, which might be due to the replacement of Yb^{3+} ions by larger La^{3+} ions or stain/stress in crystallites. Moreover, the electron diffraction patterns further indicate that all particles have the pyrochlore crystal structure, as there are two weak diffraction rings corresponding to (3,3,1) and (5,1,1) peaks, which matches well with XRD results (two diffraction rings noted in each diffraction pattern). The ceramics exhibit clear diffraction rings generated by diffraction spots due to their nano-sized particles and different crystal orientations.

3.4 Thermal conductivity

The thermal conductivities of stannate ceramics and 8YSZ are compared in Figure 6. The thermal conductivities of $La_2Sn_2O_7$, $(La_{0.7}Yb_{0.3})_2Sn_2O_7$, $(La_{0.5}Yb_{0.5})_2Sn_2O_7$, $(La_{0.3}Yb_{0.7})_2Sn_2O_7$ and $Yb_2Sn_2O_7$ pellets are 1.471 $W \cdot m^{-1} \cdot K^{-1}$, 1.063 $W \cdot m^{-1} \cdot K^{-1}$, 0.851 $W \cdot m^{-1} \cdot K^{-1}$, 1.069 $W \cdot m^{-1} \cdot K^{-1}$ and 1.736 $W \cdot m^{-1} \cdot K^{-1}$, respectively. All thermal conductivity values were corrected by their porosities, which were from 30% to 40%. Additionally, it can be seen that the thermal conductivities do not always decrease with the increase of the doping content of La^{3+} ions. The lowest point of thermal conductivity appears in $(La_xYb_{1-x})_2Sn_2O_7$ solid solution when x=0.5. However, compared with that of 8 wt.% YSZ (1.353 $W \cdot m^{-1} \cdot K^{-1}$, produced in this work following the same procedure as the reference material) and $La_2Zr_2O_7$ (1.154 $W \cdot m^{-1} \cdot K^{-1}$) ceramic pellets, all doped stannates have relatively lower thermal conductivities, which is the key advantage for TBC application. Similar thermal conductivity value (~1.4 $W \cdot m^{-1} \cdot K^{-1}$) was reported for 8YSZ produced by sol-gel method at room temperature [28], by Rauf *et al*.

In crystalline solids, phonons are the main heat carriers [29]. Stannate pellets with such low thermal conductivity cannot be just simply explained by one or two phonon scattering mechanisms. In this present work, a combination of the following factors could lead to low thermal conductivities of doped and un-doped stannates: (1) Grain boundaries can attribute to scatter phonons in nanocrystalline materials. (2) Stannates have layered and complex pyrochlore crystal structure that can efficiently scatter phonons; (3) Oxygen vacancies existing in this crystal structure would also play a role in scattering phonons.

However, in $(La_xYb_{1-x})_2Sn_2O_7$ (x=0.3, 0.5 and 0.7) solid solution, their thermal performance might be governed by more complex mechanisms. If observed from the [0,1,0] direction, pyrochlore exhibits a layer-structure, alternating by cation layers and oxygen layers; while in each oxygen layer, some oxygen atoms are displaced from their centre positions, because of the oxygen vacancies. This is one possibility to cause a decrease of thermal conductivity. It is known that there are no extra oxygen vacancies created by replacing host cations with different rare earth ions due to the same valence charge, so the phonons are possibly scattered from the substitution defects and structure disorders created by the difference of radius or mass between atoms. However, these defects could become ordered again when excessing the maximum disorder value while reaching very high level of dopants. Therefore, when doping La^{3+} ions in Yb^{3+} sites, the radius difference could cause the disorder in cation layers, and then would also affect the arrangement in oxygen layers. These disorders could have a huge effect on further scanning phonons to reduce thermal conductivity. Furthermore, $(La_{0.5}Yb_{0.5})_2Sn_2O_7$ exhibits the lowest thermal conductivity, which could be explained by the maximum disorder achieved by replacing 50 mol.% Yb^{3+} ions by La^{3+} ions. When the doping content of La^{3+} ions increases to 70 mol.%, the thermal conductivity increases to similar value as that of 30 mol.% doped sample. So when x equals 0.7, there is a new stable state for La^{3+} ions, which seems that they are newly ordered in the crystal structure again. Moreover, these disorders might also weaken the Sn-O interatomic bonding, which could not only reduce thermal conductivity but also improve CTEs. Finally, two different compositions in each $(La_xYb_{1-x})_2Sn_2O_7$ solid solution could also contribute to phonon scattering for reducing their thermal conductivities, due to the different lattice parameters and the interfaces in between.

3.5 Coefficients of thermal expansion

It has been reported that CTEs of un-doped stannates are $7\sim9\times10^{-6}$ K^{-1} [30], in good agreement with the values measured for $La_2Sn_2O_7$ and $Yb_2Sn_2O_7$ ceramic pellets in this work, which are 3.819×10^{-6} K^{-1} and 7.355×10^{-6} K^{-1} at 50°C; 7.560×10^{-6} K^{-1} and 9.035×10^{-6} K^{-1} at 950°C, respectively (Figure 7). The CTEs increase with increasing temperature but they level off at high temperatures. In Figure 7, it is shown that ceramic $La_2Sn_2O_7$ has the lowest CTE even at high temperature. The CTE of $(La_{0.5}Yb_{0.5})_2Sn_2O_7$ pellet shows a dramatic increase from 7.082×10^{-6} K^{-1} at 50°C to 13.530×10^{-6} K^{-1} at 950°C, while, the CTE values of 8YSZ are 9.860×10^{-6} ~ 13.310×10^{-6} K^{-1} from 50°C to 950°C. Moreover, $(La_{0.7}Yb_{0.3})_2Sn_2O_7$, $(La_{0.3}Yb_{0.7})_2Sn_2O_7$ and $Yb_2Sn_2O_7$ ceramic pellets have similar CTE values, approximately $7\sim9\times10^{-6}$ K^{-1}.

In term of microscopic scale, the atoms never vibrate in their equilibrium positions in imperfect crystals, so the volume expansion occurs, dependent on the temperature. From previous studies, lower CTEs in stannates might generally be resulted from the stronger bonding of Sn-O present in stannates than that of Zr-O in zirconates [30]. Lian *et al.* reported that $La_2Sn_2O_7$ have stronger covalent bonding of Sn-O than other stannates, because of larger La^{3+} ions [31]. Pyrochlore structure is usually considered as an ordered defect fluorite structure with the ordered two cations and 8a anion vacancy. However, these order structures could be changed by doping different cations on A sites, so the disorder could be created in cation layers, then these disorders would affect the bonding length between cation atoms and coordinated oxygen atoms. Therefore, the strong bonding of Sn-O would be weakened, leading to increased CTEs. Especially for $(La_{0.5}Yb_{0.5})_2Sn_2O_7$, the maximum disorders may be entirely activated at high temperature, which leads to the highest CTE values in solid solution $(La_xYb_{1-x})_2Sn_2O_7$ (x=0.3, 0.5 and 0.7). At low temperature, the level of atom vibration are

limited, thus thermal expansion is increasing with the increase of temperature. After 500^{o}C, due to the saturation of atom vibration, CTE values increase very slow, nearly being temperature independent.

4 Conclusions

Based on the study of crystal structure and ion radii, La^{3+} ions were introduced to produce crystal disorders by replacing Yb3+ ions in Yb_2Sn_2O. La^{3+} Doped $Yb_2Sn_2O_7$ materials with pyrochlore crystal structure were synthesized by sol-gel method, demonstrating lower thermal conductivity and good phase stability at higher temperature. In summary, conclusions could be drawn as follows:

1) The simulation XRD results had good agreement with experimental data. Lattice constants and relative phase contents of two different compositions in each solid solution $(La_xYb_{1-x})_2Sn_2O_7$ (x=0.3, 0.5 and 0.7) were obtained, and the lattice constants change linearly with the increase of La^{3+} ions.
2) $La_2Sn_2O_7$, $(La_{0.7}Yb_{0.3})_2Sn_2O_7$, $(La_{0.5}Yb_{0.5})_2Sn_2O_7$, $(La_{0.3}Yb_{0.7})_2Sn_2O_7$ and $Yb_2Sn_2O_7$ had lower thermal conductivities than that of 8YSZ. $(La_xYb_{1-x})_2Sn_2O_7$ (x=0.3, 0.5 and 0.7) solid solutions have much lower thermal conductivity values, around 1 $W\cdot m^{-1}\cdot K^{-1}$at room temperature.
3) Most stannates, $La_2Sn_2O_7$, $(La_{0.7}Yb_{0.3})_2Sn_2O_7$, $(La_{0.3}Yb_{0.7})_2Sn_2O_7$ and $Yb_2Sn_2O_7$, exhibited lower coefficients of thermal expansion ($7\sim9\times10^{-6}$ K^{-1}), compared with that of 8YSZ.
4) Ceramic $(La_{0.5}Yb_{0.5})_2Sn_2O_7$ pellet had the lowest thermal conductivity value (0.851 $W\cdot m^{-1}\cdot K^{-1}$) in stannates at room temperature, and higher thermal expansion coefficient (13.530×10^{-6} K^{-1}) at 950°C, compared with standard 8YSZ ceramic.

Acknowledgement

J. Wang wishes to acknowledge the studentship support from University of Nottingham and ACAE.

References

[1] L. Wang, Y. Wang, X.G. Sun, J.Q. He, Z.Y. Pan, C.H. Wang. A novel structure design towards extremely low thermal conductivity for thermal barrier coatings – Experimental and mathematical study, Mater. Des. 35 (2012) 505-517.

[2] R. Darolia. Thermal barrier coatings technology: critical review, progress update, remaining challenges and prospects, International Materials Reviews 58 (2013) 315-348.

[3] R.L. Jones, R.F. Reidy, D. Mess. Scandia, yttria-stabilized zirconia for thermal barrier coatings, Surf. Coat. Technol. 82 (1996) 70-76.

[4] J. Ilavsky, J.K. Stalick. Phase composition and its changes during annealing of plasma-sprayed YSZ, Surf. Coat. Technol. 127 (2000) 120-129.

[5] B. Sudhangshu. Thermal barrier coatings (TBCs). High Temperature Coatings. Butterworth-Heinemann, Burlington, 2007. pp. 183.

[6] M. Mrdak, M. Rakin, B. Medjo, N. Bajić. Experimental study of insulating properties and behaviour of thermal barrier coating systems in thermo cyclic conditions, Mater. Des. 67 (2015) 337-343.

[7] L. Kong, I. Karatchevtseva, M.G. Blackford, N. Scales, G. Triani. Aqueous chemical synthesis of $Ln_2Sn_2O_7$ pyrochlore-structured ceramics, J. Am. Ceram. Soc. 96 (2013) 2994-3000.

[8] X. Xie, H. Guo, S. Gong, H. Xu. Lanthanum–titanium–aluminum oxide: A novel thermal barrier coating material for applications at 1300°C, J. Eur. Ceram. Soc. 31 (2011) 1677-1683.

[9] B. Jiang, M.H. Fang, Z.H. Huang, Y.G. Liu, P. Peng, J. Zhang. Mechanical and thermal properties of $LaMgAl_{11}O_{19}$, Mater. Res. Bull. 45 (2010) 1506-1508.

[10] M. Dietrich, R. Vaßen, D. Stöver. $LaYbO_3$, A candidate for thermal barrier coating materials. 27th Annual Cocoa Beach Conference on Advanced Ceramics and Composites: A: Ceramic Engineering and Science Proceedings. John Wiley & Sons, Inc., 2008. pp. 637-643.

[11] N.P. Padture, P.G. Klemens. Low thermal conductivity in garnets, J. Am. Ceram. Soc. 80 (1997) 1018-1020.

[12] X.Q. Cao, R. Vassen, D. Stoever. Ceramic materials for thermal barrier coatings, J. Eur. Ceram. Soc. 24 (2004) 1-10.

[13] H. Zhu, D. Jin, L. Zhu, H. Yang, K. Yao, Z. Xi. A general hydrothermal route to synthesis of nanocrystalline lanthanide stannates: $Ln_2Sn_2O_7$ (Ln=Y, La–Yb), J. Alloys Compd. 464 (2008) 508-513.

[14] P.K. Schelling, S.R. Phillpot, R.W. Grimes. Optimum pyrochlore compositions for low thermal conductivity, Philos. Mag. Lett. 84 (2004) 127-137.

[15] Z. Qu, C. Wan, W. Pan. Thermophysical properties of rare-earth stannates: Effect of pyrochlore structure, Acta Mater. 60 (2012) 2939-2949.

[16] N.P. Bansal, D. Zhu. Effects of doping on thermal conductivity of pyrochlore oxides for advanced thermal barrier coatings, Mater. Sci. Eng., A 459 (2007) 192-195.

[17] M. Omini, A. Sparavigna. Effect of phonon scattering by isotope impurities on the thermal conductivity of dielectric solids, Phys. Rev. B 233 (1997) 230-240.

[18] S. Zouari, R. Ballou, A. Cheikh-Rouhou, P. Strobel. Synthesis and structure of new pyrochlore-type oxides Ln_2ScNbO_7(Ln = Pr, Nd, Eu, Gd, Dy), Mater Lett 62 (2008) 3767-3769.

[19] L.W. Finger, D.E. Cox, A.P. Jephcoat. A correction for powder diffraction peak asymmetry due to axial divergence, J. Appl. Crystallogr. 27 (1994) 892-900.

[20] T. Hagiwara, H. Yamamura, H. Nishino. Relationship between oxide-ion conductivity and ordering of oxygen vacancy in the $Ln_2Zr_2O_7$ (Ln = La, Nd, Eu) system having a pyrochlore composition, IOP Conference Series: Materials Science and Engineering 18 (2011) 132003.

[21] H. Liu, S. Li, Q. Li, Y. Li. Investigation on the phase stability, sintering and thermal conductivity of Sc_2O_3–Y_2O_3–ZrO_2 for thermal barrier coating application, Mater. Des. 31 (2010) 2972-2977.

[22] S.I. Ahmad, P. Koteshwar Rao, I.A. Syed. Sintering temperature effect on density, structural

and morphological properties of Mg- and Sr-doped ceria J. Taibah Univ. Sci. (2015) 5 (In press) doi:10.1016/j.jtusci.2015.04.003.
[23] K.E. Sickafus, L. Minervini, R.W. Grimes, J.A. Valdez, M. Ishimaru, F. Li, K.J. McClellan, T. Hartmann. Radiation tolerance of complex oxides, Science 289 (2000) 748-751.
[24] J. Matejicek, S. Sampath, P.C. Brand, H.J. Prask. Quenching, thermal and residual stress in plasma sprayed deposits: NiCrAlY and YSZ coatings, Acta Mater. 47 (1999) 607-617.
[25] Z. Fu, H.K. Yang, B.K. Moon, B.C. Choi, J.H. Jeong. $La_2Sn_2O_7:Eu^{3+}$ micronanospheres: hydrothermal synthesis and luminescent properties, Cryst. Growth Des. 9 (2008) 616-621.
[26] M.G. Brik, A.M. Srivastava. Pyrochlore structural chemistry: predicting the lattice constant by the ionic radii and electronegativities of the constituting ions, J. Am. Ceram. Soc. 95 (2012) 1454-1460.
[27] B.J. Kennedy, B.A. Hunter, C.J. Howard. Structural and bonding trends in tin pyrochlore oxides, J. Solid State Chem. 130 (1997) 58-65.
[28] A. Rauf, Q. Yu, L. Jin, C. Zhou. Microstructure and thermal properties of nanostructured lanthana-doped yttria-stabilized zirconia thermal barrier coatings by air plasma spraying, Scr. Mater. 66 (2012) 109-112.
[29] G.A. Slack, D.W. Oliver. Thermal conductivity of garnets and phonon scattering by rare-earth ions, Phys. Rev. B 4 (1971) 592-609.
[30] J. Feng, B. Xiao, R. Zhou, W. Pan. Thermal expansion and conductivity of $RE_2Sn_2O_7$ (RE=La, Nd, Sm, Gd, Er and Yb) pyrochlores, Scr. Mater. 69 (2013) 401-404.
[31] J. Lian, K.B. Helean, B.J. Kennedy, L.M. Wang, A. Navrotsky, R.C. Ewing. Effect of structure and thermodynamic stability on the response of lanthanide stannate pyrochlores to ion beam irradiation, J. Phys. Chem. B 110 (2006) 2343-2350.

Table 1. The lattice constants and relative phase contents of different compositions in $(La_xYb_{1-x})_2Sn_2O_7$ (x=0.3, 0.5 and 0.7) solid solutions.

Sample ID	**Composition**	**Lattice Constant (Å)**	**Relative Phase Content (%)**
$(La_{0.7}Yb_{0.3})_2Sn_2O_7$	C1	10.655	73.77%
	C2	10.585	26.23%
$(La_{0.5}Yb_{0.5})_2Sn_2O_7$	C3	10.570	28.10%
	C4	10.483	71.90%
$(La_{0.3}Yb_{0.7})_2Sn_2O_7$	C5	10.525	21.72%
	C6	10.432	78.28%

List of figure captions

Figure 1. **(a)** Complex pyrochlore crystal structure of $A_2B_2O_7$ (A=La^{3+}, Yb^{3+} or La^{3+} and Yb^{3+} mixed together; B=Zr^{4+}) if observed from [0,1,0] direction; **(b)** Cationic sub-lattice of pyrochlore, where atom A is in yellow colour, atom B in red colour and atom O in blue colour.

Figure 2. **(a)**: XRD patterns of ceramic $La_2Zr_2O_7$, $La_2Sn_2O_7$, $(La_{0.7}Yb_{0.3})_2Sn_2O_7$, $(La_{0.5}Yb_{0.5})_2Sn_2O_7$, $(La_{0.3}Yb_{0.7})_2Sn_2O_7$, and $Yb_2Sn_2O_7$ powders detected at room temperature and small amount of La_2O_3 presented in $La_2Sn_2O_7$, $(La_{0.7}Yb_{0.3})_2Sn_2O_7$, and $(La_{0.5}Yb_{0.5})_2Sn_2O_7$ ceramics; Graphs **(b)** enlarged from **(a)**, where (4,0,0), (4,4,0) and (6,2,2) peaks shift to higher angle with decreasing La ions content in $(La_xYb_{1-x})_2Sn_2O_7$ (x=0.3, 0.5 and 0.7) solid solution, due to smaller radius of Yb^{3+} ions. Furthermore, solid solutions $(La_xYb_{1-x})_2Sn_2O_7$ (x=0.3, 0.5 and 0.7) have two similar compositions that can be identified from (4,4,0) and (6,2,2) widen peaks, and C1, C2, C3, C4, C5 and C6 represent different compositions, respectively.

Figure 3. The good agreement between the calculative simulation XRD data and the experimental XRD pattern for samples $(La_{0.7}Yb_{0.3})_2Sn_2O_7$ **(a)**, $(La_{0.5}Yb_{0.5})_2Sn_2O_7$ **(b)** and $(La_{0.3}Yb_{0.7})_2Sn_2O_7$ **(c)**, where Diff refers to the difference between the calculative (Calc) and observed (Obs) data. And their lattice constants and relative phase were also calculated.

Figure 4. The linear changes of lattice constants of $(La_xYb_{1-x})_2Sn_2O_7$ (x=0.3, 0.5 and 0.7) solid solution with the increasing contents of La^{3+} dopants.

Figure 5. Bright field TEM images of **(a)** $Yb_2Sn_2O_7$, **(b)** $(La_{0.3}Yb_{0.7})_2Sn_2O_7$, **(c)** $(La_{0.7}Yb_{0.3})_2Sn_2O_7$ and **(d)** $(La_{0.5}Yb_{0.5})_2Sn_2O_7$ powders. The insets are the higher magnification TEM images and electron diffraction patterns at selected area for each sample, respectively.

Figure 6. Thermal conductivity versus doping content of La^{3+} ions in $(La_xYb_{1-x})_2Sn_2O_7$ (x=0.3, 0.5 and 0.7) solid solution.

Figure 7. Coefficients of thermal expansion versus temperature for $La_2Sn_2O_7$, $(La_{0.7}Yb_{0.3})_2Sn_2O_7$, $(La_{0.5}Yb_{0.5})_2Sn_2O_7$, $(La_{0.3}Yb_{0.7})_2Sn_2O_7$ and $Yb_2Sn_2O_7$ pellets.

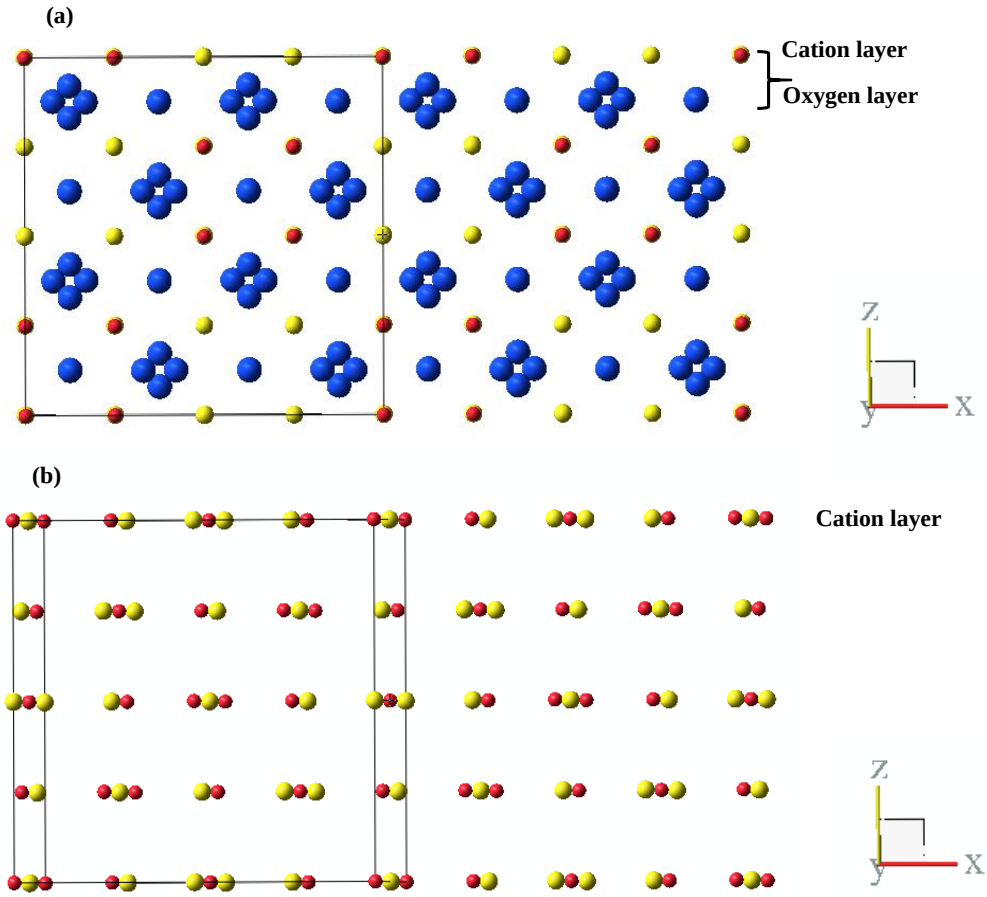

Figure 1. **(a)** Complex pyrochlore crystal structure of $A_2B_2O_7$ (A=La^{3+}, Yb^{3+} or La^{3+} and Yb^{3+} mixed together; B=Zr^{4+}) if observed from [0,1,0] direction; **(b)** Cationic sub-lattice of pyrochlore, where atom A is in yellow colour, atom B in red colour and atom O in blue colour.

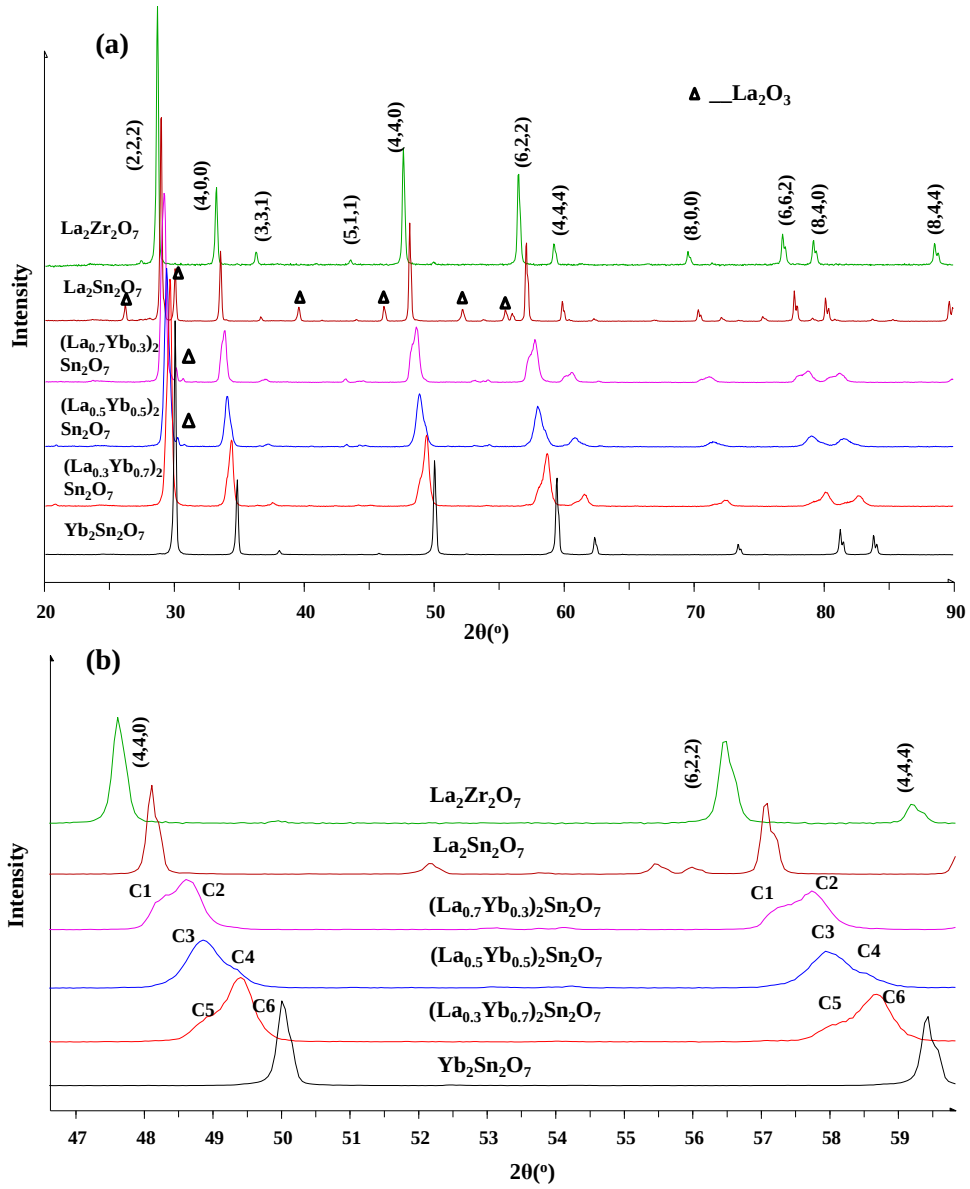

Figure 2. **(a)**: XRD patterns of ceramic $La_2Zr_2O_7$, $La_2Sn_2O_7$, $(La_{0.7}Yb_{0.3})_2Sn_2O_7$, $(La_{0.5}Yb_{0.5})_2Sn_2O_7$, $(La_{0.3}Yb_{0.7})_2Sn_2O_7$, and $Yb_2Sn_2O_7$ powders detected at room temperature and small amount of La_2O_3 presented in $La_2Sn_2O_7$, $(La_{0.7}Yb_{0.3})_2Sn_2O_7$, and $(La_{0.5}Yb_{0.5})_2Sn_2O_7$ ceramics; Graphs **(b)** enlarged from **(a)**, where (4,0,0), (4,4,0) and (6,2,2) peaks shift to higher angle with decreasing La ions content in $(La_xYb_{1-x})_2Sn_2O_7$ (x=0.3, 0.5 and 0.7) solid solution, due to smaller radius of Yb^{3+} ions. Furthermore, solid solutions $(La_xYb_{1-x})_2Sn_2O_7$ (x=0.3, 0.5 and 0.7) have two similar compositions that can be identified from (4,4,0) and (6,2,2) widen peaks, and C1, C2, C3, C4, C5 and C6 represent different compositions, respectively.

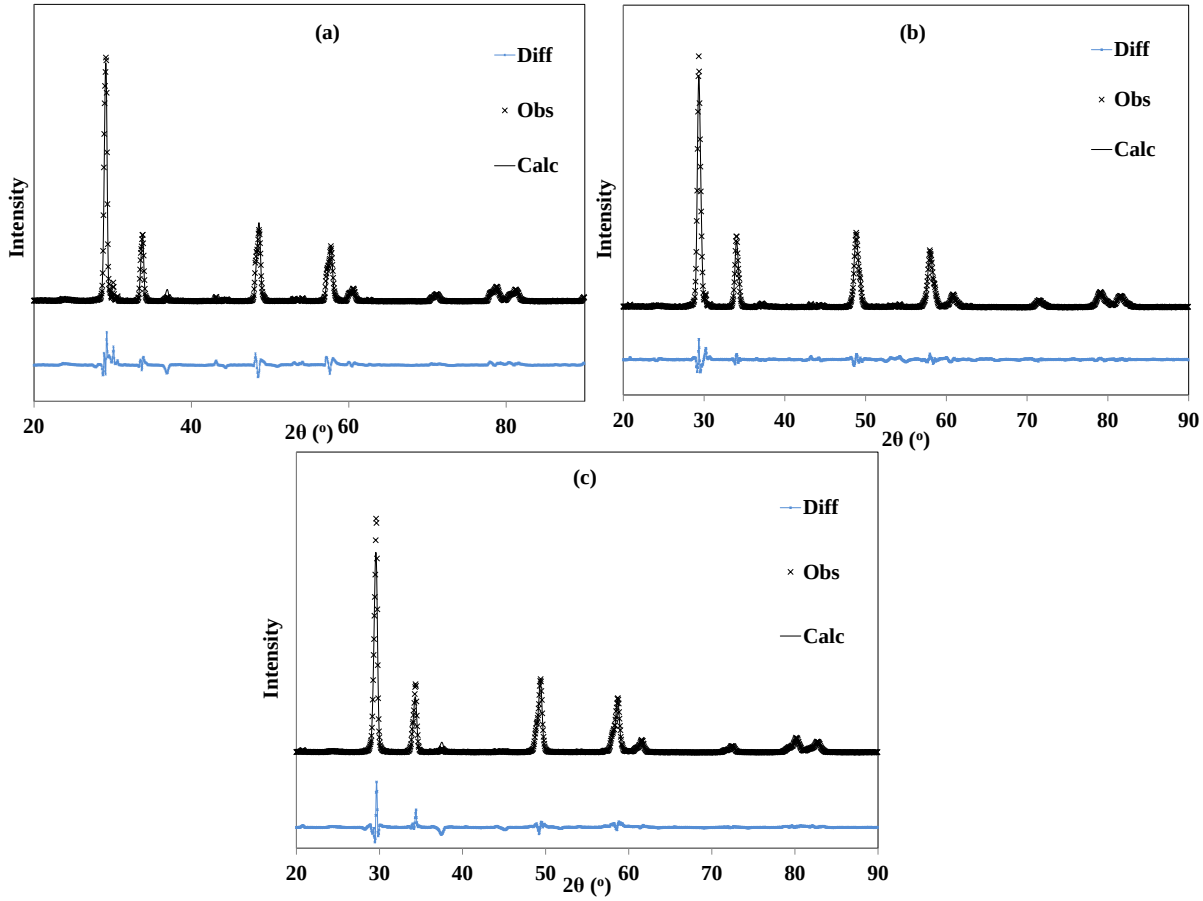

Figure 3. The good agreement between the calculative simulation XRD data and the experimental XRD pattern for samples $(La_{0.7}Yb_{0.3})_2Sn_2O_7$ **(a)**, $(La_{0.5}Yb_{0.5})_2Sn_2O_7$ **(b)** and $(La_{0.3}Yb_{0.7})_2Sn_2O_7$ **(c)**, where Diff refers to the difference between the calculative (Calc) and observed (Obs) data. And their lattice constants and relative phase were also calculated.

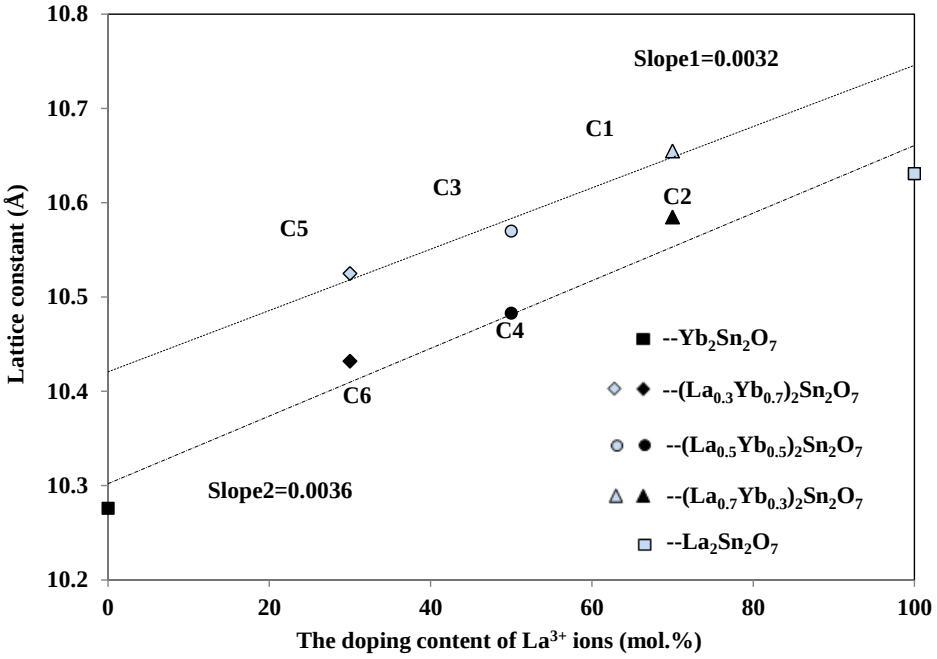

Figure 4. The linear changes of lattice constants of $(La_xYb_{1-x})_2Sn_2O_7$ (x=0.3, 0.5 and 0.7) solid solution with the increasing contents of La^{3+} dopants.

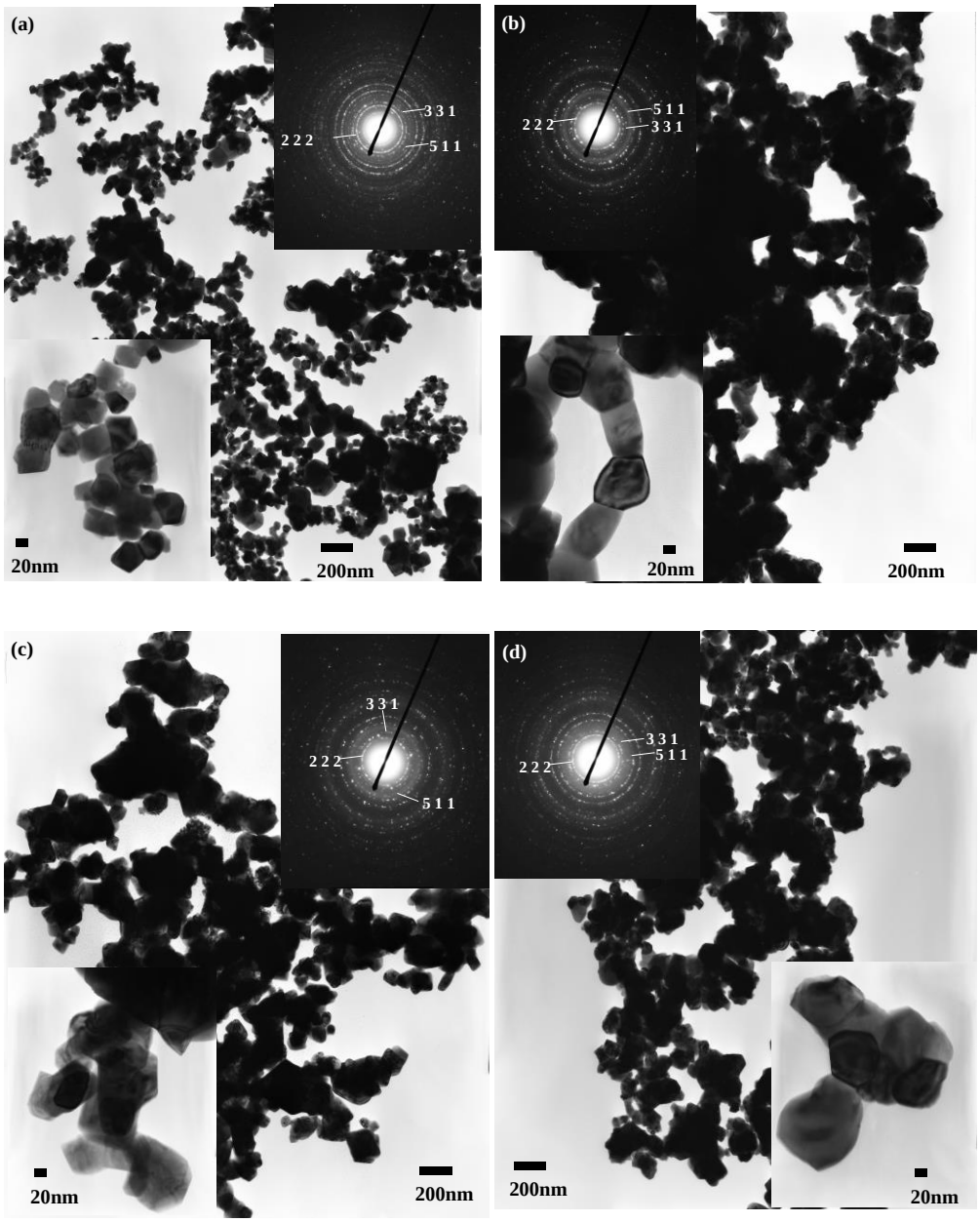

Figure 5. Bright field TEM images of **(a)** $Yb_2Sn_2O_7$, **(b)** $(La_{0.3}Yb_{0.7})_2Sn_2O_7$, **(c)** $(La_{0.7}Yb_{0.3})_2Sn_2O_7$ and **(d)** $(La_{0.5}Yb_{0.5})_2Sn_2O_7$ powders. The insets are the higher magnification TEM images and electron diffraction patterns at selected area for each sample, respectively.

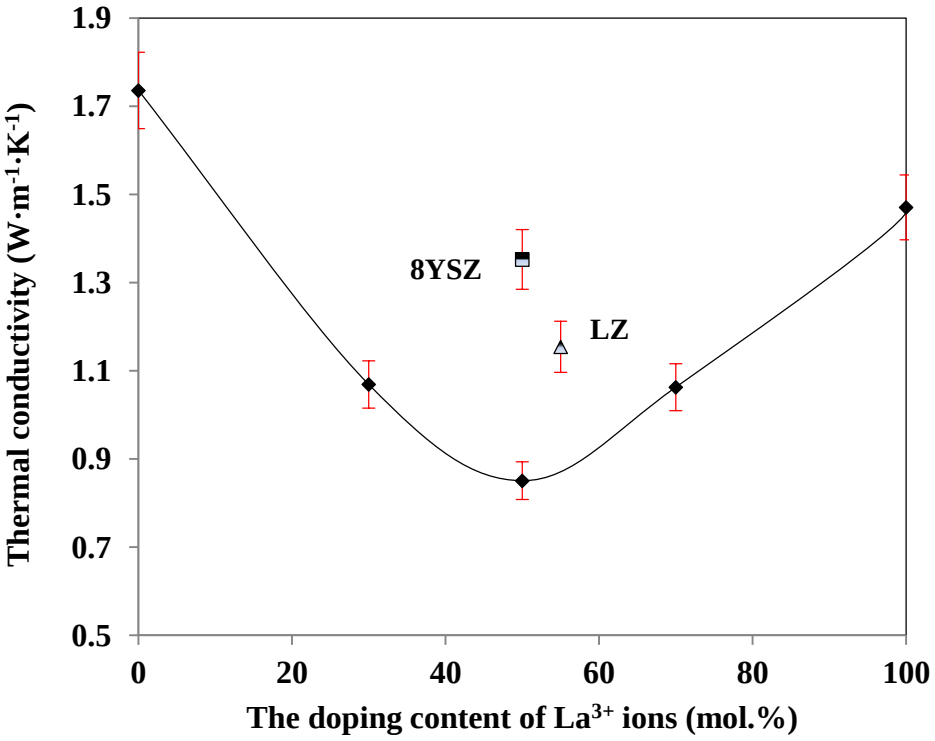

Figure 6. Thermal conductivity versus doping content of La^{3+} ions in $(La_xYb_{1-x})_2Sn_2O_7$ (x=0.3, 0.5 and 0.7) solid solution.

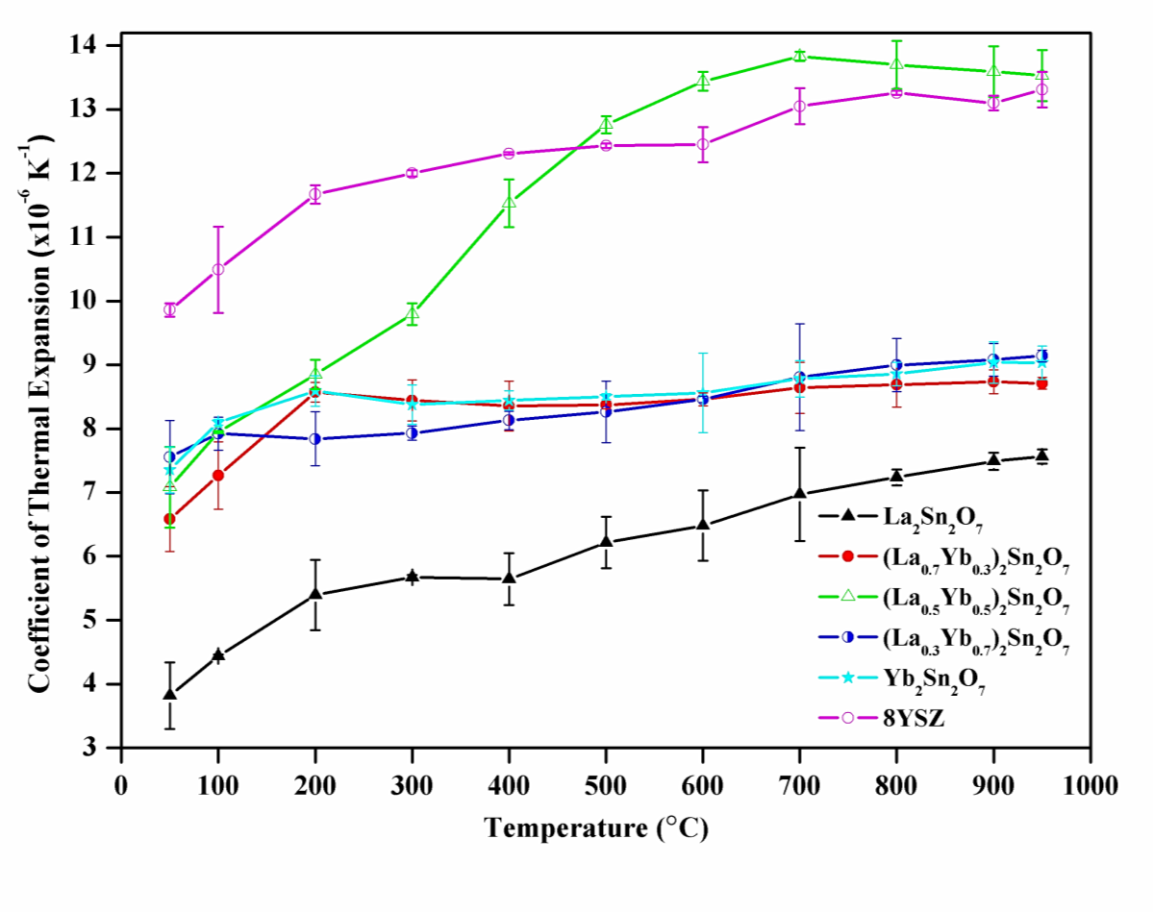

Figure 7. Coefficients of thermal expansion versus temperature for $La_2Sn_2O_7$, $(La_{0.7}Yb_{0.3})_2Sn_2O_7$, $(La_{0.5}Yb_{0.5})_2Sn_2O_7$, $(La_{0.3}Yb_{0.7})_2Sn_2O_7$ and $Yb_2Sn_2O_7$ pellets.